Linear-polarization–gradient-phase coupling

Shangdong Zhao,[1,*] Yu Liu,[1,*] Kai Niu,[2] and Shaohua Tao[1,3,†]
[1]*School of Physics and Electronics, Central South University, Changsha 410083, China*
[2]*School of Mechanical and Electrical Engineering, Central South University, Changsha 410083, China*
[3]*Hunan Key Laboratory of Nanophotonics and Devices, Central South University, Changsha 410083, China*

(Received 6 May 2022; accepted 23 September 2022; published 10 October 2022)

As the fundamental information of light, phase, and polarization have been widely studied and applied. We find that the linear polarization-gradient phase coupling can occur in a specific condition, i.e., the linear polarization of an incident beam with uniform phase can be converted under the tight focusing to the nearly linear gradient phase of the output beam. In this article we have proved both theoretically and experimentally that a tightly focused linearly polarized beam with uniform phase can be converted into a beam with gradient phase, and the tightly focused beam has been found to transport particles automatically owing to the possession of the gradient phase force.

DOI: 10.1103/PhysRevA.106.043506

I. INTRODUCTION

It is well known that the angular momentum (AM) of light can be categorized into spin angular momentum (SAM) and orbital angular momentum (OAM), which are carried by the circular polarization and helical phase of light, respectively. In the interaction of light with matter, the circularly polarized light with SAM can make a birefringent crystal spin [1], whereas a vortex beam with OAM can make particles rotate around the beam's axis [2–4]. In recent years, the spin-orbit interaction has been of great interest and gradually became an indispensable part of modern optics [5–9]. Optical spin-to-orbital AM conversion can occur in some special conditions. For instances, by exploiting symmetric nanorings possessing continuous gradient phase, the researchers realized highly efficient spin-to-vortex conversion [10]. The spin-to-orbital coupling has also been achieved successfully in metasurfaces [11,12] and optical fibers [13]. In a highly focused system, a circularly polarized beam partly transfers its SAM to the OAM, which leads to the generation of a helical phase in the longitudinal component of the electric field [14–16]. Under the same condition, it was found that the SAM of an elliptically polarized vortex beam had been converted to the OAM, and the elliptical light spots presented in the focal plane could be changed by adjusting certain parameters of the elliptically polarized vortex beam [17]. Different from the traditional spin-to-orbit AM transfer in an asymmetrical anisotropic medium, the novel spin-orbit mapping phenomena in the weakly guiding few-mode fiber have been found recently [18]. However, only the spin-orbit conversion in specific conditions has been found and studied previously. We found that a linear polarization-gradient phase coupling can occur exactly in a homogeneous and isotropic medium when a linearly polarized light is tightly focused by a high numerical aperture (NA) and magnification objective lens. Actually, it is shown that gradient phase in a beam of light can be used to create an optical force transverse to the optical axis [19]. Furthermore, optical trajectories with gradient phase and designed intensity distributions were generated by the complex-amplitude beam shaping methods [20–22], which were applied to generate the desired optical beams to realize the automatic transmission of particles [23,24]. Optical forces arising from the polarization can also produce a force on particles in the transverse plane [25,26]. Several findings were reported in literature, for instance, the orientation of a trapped calcite particle was controlled by linearly polarized light. Moreover, the researchers found that a particle with a specific shape could also be aligned by linearly polarized light even the particle was not birefringent [27–30].

In this article we realized the coupling between the linear polarization and the gradient phase by tightly focusing a linearly polarized beam with a high NA and magnification of 100 objective lens. Furthermore, we designed a line-shaped beam used for the optical manipulation. The conversion from the linear polarization of the line-shaped beam with uniform phase to the gradient phase of the focused beam was verified experimentally.

II. THEORY AND SIMULATION

The simulation method is described in the following. In a tightly focusing system, it was found that there is a conversion between the circular polarization state and the helical phase distribution. The conversion can be taken as the coupling between the SAM per photon of the circularly polarized beam and the OAM per photon of the vortex beam. In this regard, it is deductible that the conversion between the linear polarization and the photonic momentum may occur. We set a linearly polarized beam as the incident beam that is incident on the objective lens. The electric field of the incident beam can be

*These authors contributed equally to this work.
†eshtao@csu.edu.cn

expressed as Eq. (1),

$$\boldsymbol{E}(\gamma,\theta,\phi) = A(\gamma,\theta,\phi)[\cos(\delta)\boldsymbol{e_x} + \sin(\delta)\boldsymbol{e_y}], \tag{1}$$

where $A(\gamma,\theta,\phi)$ represents the complex amplitude of the incident beam, which contains both the amplitude information and the phase information. $\cos(\delta)\boldsymbol{e_x} + \sin(\delta)\boldsymbol{e_y}$ determines the linear polarization, θ and ϕ are the variables in the spherical coordinates, δ indicates the angle of the linearly polarized beam relative to the x direction, $\boldsymbol{e_x}$ and $\boldsymbol{e_y}$ represent the unit vectors along the x and y directions, respectively, and $\gamma = f\sin\theta$. So $A(\gamma,\theta,\phi) = A(\theta,\phi)$, and f is the focal length of the objective lens. Since the focal length f is a constant, γ is not an independent variable. Therefore, $E(\gamma,\theta,\phi)$ can be simplified as $E(\theta,\phi)$, and $E(\gamma,\theta,\phi)$ is meant to represent a two-dimensional field.

On the basis of the coordinate system transformation based on the Debye integrals [31] and Wolf's theory [32,33], the tight focusing process with an objective lens for a linearly polarized beam can be illustrated with Fig. 1, and the origin of the coordinate system is located at point o. The x, y, and z components of the electric field of the focused linearly polarized beam are written as Eq. (2),

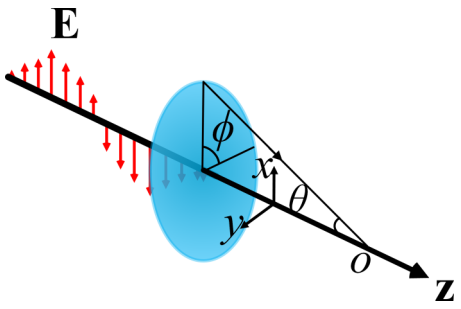

FIG. 1. Schematic illustrating the tight focusing process of a linearly polarized beam, o is the origin of the coordinate system.

$$\begin{aligned}
E_x(r,\varphi,z) &= \frac{-ikf}{2\pi}\int_0^{2\pi}\int_0^{\theta_{\max}}\left[\begin{array}{l}\cos^{1/2}\theta A(\theta,\phi)[\cos(\delta-\phi)\cos\phi\cos\theta - \sin(\delta-\phi)\sin\phi] \\ \times\exp\{ik[-r\sin\theta\cos(\phi-\varphi)+z\cos\theta]\}\end{array}\right]\sin\theta d\theta d\phi \\
E_y(r,\varphi,z) &= \frac{-ikf}{2\pi}\int_0^{2\pi}\int_0^{\theta_{\max}}\left[\begin{array}{l}\cos^{1/2}\theta A(\theta,\phi)[\cos(\delta-\phi)\sin\phi\cos\theta + \sin(\delta-\phi)\cos\phi] \\ \times\exp\{ik[-r\sin\theta\cos(\phi-\varphi)+z\cos\theta]\}\end{array}\right]\sin\theta d\theta d\phi \\
E_z(r,\varphi,z) &= \frac{-ikf}{2\pi}\int_0^{2\pi}\int_0^{\theta_{\max}}\left[\begin{array}{l}\cos^{1/2}\theta A(\theta,\phi)\exp\{ik[-r\sin\theta\cos(\phi-\varphi)+z\cos\theta]\} \\ \times\cos(\delta-\phi)\end{array}\right]\sin^2\theta d\theta d\phi,
\end{aligned} \tag{2}$$

where r, φ and z are the cylindrical coordinates of an observation point, $k = 2\pi/\lambda$ is the wave vector, and λ is the wavelength of the beam. $\theta_{\max} = \arcsin(\mathrm{NA}/n_1)$ is the maximal angle determined by the NA of the objective lens, where $n1$ represents the refractive index of the medium surrounding the lens.

The irradiance of the focused beam is $I = |E_x|^2 + |E_y|^2 + |E_z|^2$, and the phase of the focused beam is $\Psi = \mathrm{Arg}(E_xU_x^* + E_yU_y^* + E_zU_z^*)$ [34], where $*$ denotes a complex conjugate, and U_x, U_y, and U_z are expressed in Eq. (3), which is is a general formula for calculating the phase of the focused beam. In general cases, U_i is a complex, but for the case that the incident beam is linearly polarized, U_i is real:

$$\begin{aligned}
U_x &= \cos(\delta-\phi)\cos\phi\cos\theta - \sin(\delta-\phi)\sin\phi \\
U_y &= \cos(\delta-\phi)\sin\phi\cos\theta + \sin(\delta-\phi)\cos\phi \\
U_z &= \cos(\delta-\phi)\sin\theta.
\end{aligned} \tag{3}$$

We set the incident beam as a collimated beam, i.e., a plane wave, whose amplitude and phase are uniform. As the phase is uniform, the number of nodes for the spiral phase is not involved in the input beam of the system. The polarization status of the plane wave is set as linear. In our calculation the amplitude is set as 1 and the phase is π. Thus, substituting the linearly polarized plane wave into Eq. (2), we obtain the x, y, and z components of the electric field of the tightly focused beam as Eq. (4) which is a special case of Eq. (2).

$$\begin{aligned}
E_x(r,\varphi,z) &= -\frac{ikf\exp(i\pi)}{2}\int_0^{\theta_{\max}}\left[\begin{array}{l}\sin\theta\cos^{1/2}\theta\exp(ikz\cos\theta)\times\{J_0(kr\sin\theta)\cos\delta\cos\theta \\ -J_2(kr\sin\theta)\cos2\phi - J_2(kr\sin\theta)\sin2\phi \\ +J_2(kr\sin\theta)\sin2\phi\sin\delta + J_2\cos\delta(kr\sin\theta)\cos2\theta \\ +J_0(kr\sin\theta)\cos\delta\}\end{array}\right]d\theta \\
E_y(r,\varphi,z) &= -\frac{ikf\exp(i\pi)}{2}\int_0^{\theta_{\max}}\left[\begin{array}{l}\sin\theta\cos^{1/2}\theta\exp(ikz\cos\theta)\times\{J_0(kr\sin\theta)\cos\delta\cos\theta \\ -J_2(kr\sin\theta)\cos2\phi - J_2(kr\sin\theta)\sin2\phi \\ -J_2(kr\sin\theta)\sin2\phi\sin\delta - J_2\cos\delta(kr\sin\theta)\cos2\theta \\ -J_0(kr\sin\theta)\cos\delta\}\end{array}\right]d\theta \\
E_z(r,\varphi,z) &= kf\exp(i\pi)\int_0^{\theta_{\max}}\left[\begin{array}{l}\sin^2\theta\cos^{1/2}\theta\times\{J_1\cos\delta\cos\phi(kr\sin\theta) \\ +J_1\sin\delta\sin\phi(kr\sin\theta)\}\end{array}\right]d\theta,
\end{aligned} \tag{4}$$

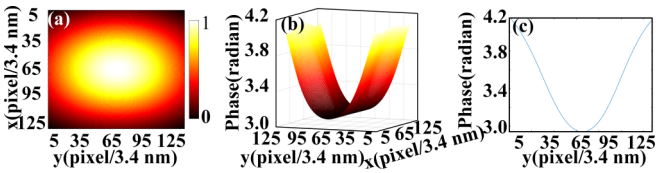

FIG. 2. (a) Intensity and (b) 3D phase distributions of the tightly focused linearly polarized plane wave in the focal plane. (c) The plot cutting along the y direction when $x = 65$ pixels(units of ε) of the phase distribution of the focused plane wave.

where J_0, J_1 and J_2 are the zeroth-order, the first-order and the second-order Bessel functions of the first kind, respectively.

We have run numerical simulations based on Eqs. (1)–(4). In the simulation, we set $\delta = \pi/2$ to keep the orientation of the linear polarization of the incident plane wave along the y direction. The relevant parameters for the simulation were $\lambda = 532$ nm, $f = 0.16$ nm, and NA $= 1.3$. The total number of the sampling points of the input plane was $N_X \times N_Y = 128 \times 128$ pixels (units of Δ) with the pixel pitch $\Delta = 300$ nm. The total number of the sampling points of the output plane was $n_x \times n_y = 128 \times 128$ pixels(units of ε) with the pixel pitch $\varepsilon = 3.4$ nm. The resolutions of the respective planes in the simulation are the sizes of the pixels in the corresponding planes. Figures 2(a) and 2(b) show the simulated intensity and three-dimensional (3D) phase distributions of the tightly focused beam in the focal plane, respectively. It is worth noting that the phase distribution in Fig. 2(c) is taken from the line cutting along the y direction when $x = 65$ pixels(units of ε), where the light is the strongest. It can be observed from Fig. 2(b) that the plots of the other cutting lines of the phase distributions present the similar profiles to that in Fig. 2(c). The phase distribution exhibits a U-shaped phase gradients ranging from $1.3\,\pi$ to π and from π to $1.3\,\pi$, which are nearly quadratic and symmetrical to the central position of the plot. The total range of the phase gradients is approximately $0.6\,\pi$. In the simulation, we also found that when we rotated the orientation of the linear polarization of the incident beam by 90 degrees, the phase profile of the focused beam would rotate by 90 degrees, too. The possession of the phase gradients of the linearly polarized beam implies the coupling between the linear polarization and the gradient phase under the condition of tight focusing. As the spot of the focused plane wave is small, it is difficult to measure the phase distribution experimentally. To verify the coupling mechanism experimentally, we designed a line-shaped beam, which has uniform intensity and phase distributed in a straight line. When the line-shaped beam is tightly focused by a high NA and magnification objective lens, the focused beam would have phase gradients along the line pattern, and particles could be trapped and moved automatically along the line pattern [35]. Thus, the possession of the gradient phase of the focused beam can be proven with the automatic movement of the trapped particles. In the simulations, the total number of the sampling points of the input plane was $N_X \times N_Y = 128 \times 128$ pixels (units of Δ) with the pixel pitch $\Delta = 300$ nm. The total number of the sampling points of the output plane was $n_x \times n_y = 128 \times 128$ pixels (units of σ) with the pixel pitch $\sigma = 34$ nm. We set $\delta = \pi/2$ to keep the orientation of the linear polarization of the incident

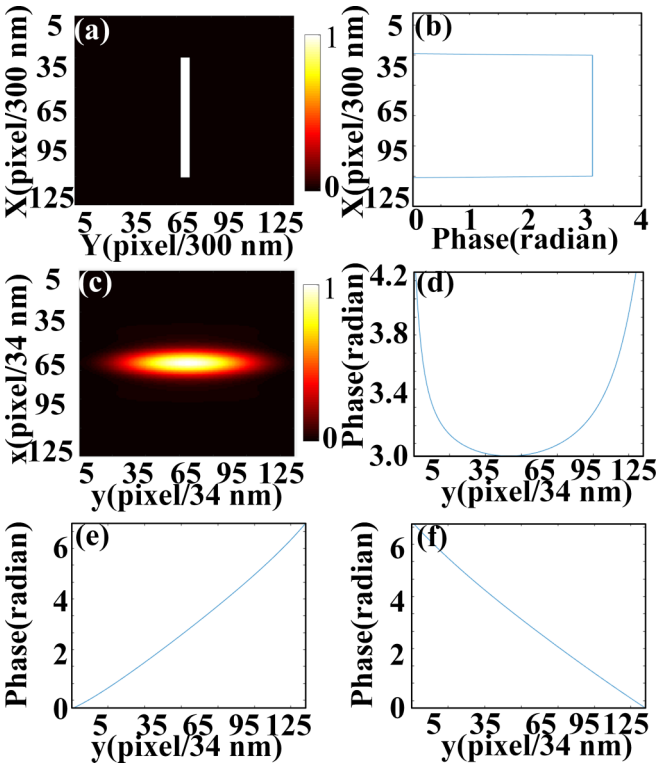

FIG. 3. (a) Intensity and (b) phase distributions of the linearly polarized line-shaped beam incident to an objective lens. (c) Intensity and (d) phase distributions of the tightly focused beam. (e) Phase distribution of the tightly focused beam when the incident beam placed 2 pixels (units of Δ) left in the input plane. (f) Phase distribution of the tightly focused beam when the incident beam placed 2 pixels (units of Δ) right in the input plane.

beam consistent with the line direction. Both the intensity and phase distributions of the incident beam are uniform. The phase of the incident line-shaped beam is π, and the size of the incident beam is 5 pixels (units of Δ) $\times$ 80 pixels (units of Δ). Figures 3(a) and 3(b) display the intensity and phase distributions of the line-shaped beam incident to the objective, respectively. In Fig. 3(b) the phase distribution is plotted along the line parallel to the X direction when $Y = 65$ pixels (units of Δ). After tight focusing through a high NA objective lens, the intensity and phase distributions of the focused beam in the focal plane are shown in Figs. 3(c) and 3(d), respectively. The incident beam is deliberately set as long and thin, so the long direction is tightly focused, but for the thin direction, the strong diffraction causes the elongation of the focused beam. The incident beam is elongated along x and polarized along y, so that the focused beam is elongated along y. Thus, the intensity and phase profiles of the focused beam are distributed along the y direction instead of the x direction. It can be seen from Fig. 3(c) that the intensity distribution of the focused beam maintains the line shape but is a little expanded due to diffraction. The plot of the phase in Fig. 3(d) is taken from the cutting line along the y direction when $x = 65$ pixels(units of σ). It can be observed from Fig. 3(d) that the focused beam has a U-shaped phase gradient which also ranges from $1.3\,\pi$ to π and then from π to $1.3\,\pi$. Compared with those of the focused plane wave, the phase gradients are steeper in the two ends

and become nearly flat in the middle of the focused beam. For a completely symmetrical output beam, both the position and the incident beam itself are required to be symmetric strictly. However, due to the grid sampling in the simulation, the incident beam is difficult to be positioned symmetrically in the input plane. Thus, even though the incident beam is symmetric, the asymmetric position of the incident beam can still lead to an asymmetric output beam. Moreover, we can observe that the size of the incident beam affects the profile of the phase gradient of the focused beam, which results in the different U shapes in Figs. 2(c) and 3(d), respectively.

The phase gradient distribution of the focused beam in the focal plane is also influenced by the position of the incident linearly polarized line-shaped beam in the input plane. We placed the incident beam 2 pixels(units of Δ) left from the position of $Y = 65$ pixels (units of Δ) in the input plane. The size and direction of the linear polarization of the incident line-shaped beam was unchanged. Figs. 3(e) show the corresponding phase distribution of the focused beams in the focal plane. It can be seen that the focused beam has unidirectional phase gradient ranging from 0 to 2 π, which increases almost linearly from the left to the right of the line pattern.

The incident linearly polarized line-shaped beam was shifted 2 pixels (units of Δ) right from the position of $Y = 65$ pixels (units of Δ) in the input plane whereas the other parameters were unchanged. After tight focusing, the phase distribution of the focused beams in the focal plane is shown in Fig. 3(f). The focused beam also has unidirectional phase gradient ranging from 2 π to 0, which decreases linearly from the left to the right of the beam. In Figs. 2(c) and 3(d), the total phase changes are almost the same, a roughly 1 rad phase shift between the edge of the beam and the center. However, the total phase changes in Figs. 3(e) and 3(f) are much greater, about 2π rad phase shift. In Fig. 2(c), the phases are nearly linear on the left of $y = 60$ and on the right of $y = 70$, respectively. In Fig. 3(d), the phases are nearly linear on the left of $y = 45$ and on the right of $y = 60$, respectively. In Figs. 3(e) and 3(f), the phases are nearly linear in the whole regions. When we shifted the incident beam left and right from the symmetrical position with more than 2 pixels (units of Δ), it was found that the ranges of the phase gradients of the focused beams in the focal plane increased to up to 14 π in our simulation.

When we increased the length of the incident line-shaped beam in the simulation, we found that the length of the beam in the focal plane was shorter accordingly, but the range of the phase gradient of the focused beam kept unchanged. When we increased the width of the incident line-shaped beam, we found that the focused beam became narrower accordingly, and the range of the phase gradient of the focused beam kept unchanged, but the slope of the phase gradient was varied. Moreover, the change of the orientation of the linear polarization of the incident line-shaped beam would change the direction of the phase gradient of the focused beam.

III. EXPERIMENTAL RESULTS

The experimental setup for optical manipulation is shown in Fig. 4, which mainly consisted of a laser, a spatial light modulator (SLM) and an imaging and observing system. The laser emitted a coherent and linearly polarized beam. However, to ensure the high linear polarization, we still inserted a polarizer to the optical path. The laser beam was collimated firstly and incident to the SLM, which modulated the beam and reconstructed the line-shaped beam. Then, the beam was reflected by a dichroic mirror (DM) and focused by an inverted microscope comprising a 100 times oil-immersion objective lens (N.A 1.3), and a charge coupled device (CCD) connected to the computer was employed to capture the real-time view of the sample stage illuminated by an illuminator, the thickness and the diameter of the sample stage are 120 μm and 9 mm, respectively. The lenses L1, L2, L3, and L4 were used to expand and collimate the beam. Note that, we used two half-wave plates (HWPs) in our optical path, the first one was applied to change the polarization orientation of the beam incident to the SLM, and the second one was used to adjust the polarization orientation of the reconstructed beam. In the experiment, the orientations of the linear polarization and the line shape of the reconstructed beam on the sample stage of the optical tweezers were adjusted as aligned.

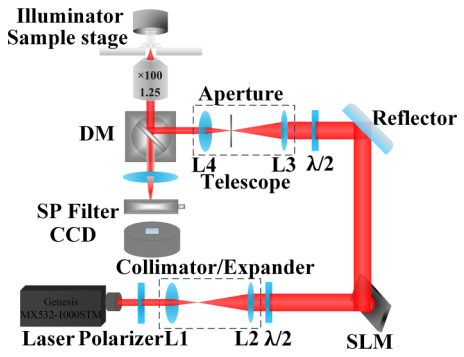

FIG. 4. Optical manipulation system for the verification of the linear polarization-gradient phase coupling. Laser: Coherent Genesis, 1.0 W with wavelength of 532 nm and adjustable laser power, $\lambda/2$: half-wave plate, SLM: Spatial light modulator (CAS MICROSTAR, FSLM-HD70-VIS, phase type, 1920 pixels $\times$ 1080 pixels, 8 μm times 8 μm, reflective type), CCD: Charge-coupled device, SP Filter: Short-pass filter, DM: Dichroic mirror, focal lengths of the lenses: fL1 = 30 mm, fL2 = 300 mm, fL3 = 300 mm, fL4 = 100 mm.

In the experiments [36], 5 μm silica beads, homogeneous in density and isotropic, were diluted in deionized water with a refractive index of 1.33 and used for the optical trapping objects. The wavelength of the laser beam is 532 nm. We used the oil-immersion objective lens, and there was no direct contact between the objective lens and particles which were immersed in water. $\theta_{\max} = \arcsin(\mathrm{NA}/n_1)$, where n_1 represents the refractive index of the medium surrounding the lens. The NA of the objective lens can reach to 1.3. The reconstructed line-shaped beam patterns, which were designed by the complex-amplitude beam shaping methods [20–22], on the sample stage of the microscope system are shown in Fig. 5. Figure 5(a) shows the reconstructed beam pattern when the beam was incident to the center of the objective lens. When the input beam was incident to the upper or the lower parts of the objective lens, the output beam patterns are obtained and shown in Figs. 5(b) and 5(c), respectively. The lengths of the line patterns in Figs. 5(a)–5(c) are about 38,

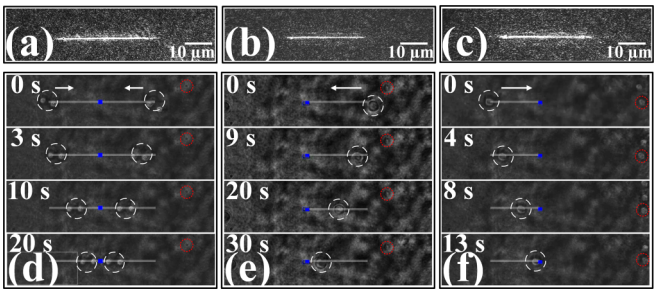

FIG. 5. Patterns of the focused linearly polarized line-shaped beam on the sample stage of the microscope when the incident beam placed in the (a) center, (b) upper and (c) lower parts of the objective lens. (d)–(f) The automatic transportations of 5 μm silica beads trapped by the tightly focused linearly polarized line-shaped beams. The silica beads are marked with white dashed circles, and the red dashed circles mark the reference beads, which are relatively motionless and used for the reference of the displaced positions of the moving particles. The white arrow denotes the transportation direction. The time sequences for the transportations are marked in the left of the images. The blue dot indicates the location where the particles stop moving. The scale bar is 10 μm.

23, and 23 μm, respectively. The beam pattern in Fig. 5(a) was designed as longer for the convenience of observing the double-way movements of the trapped particles, as the phase gradient of the focused line-shaped beam was U-shaped in this case. In the experiment, we set the laser power as 800 mW and made the polarization orientation consistent with the beam line by using the polarizer and HWPs. As shown in Fig. 5(d), the beam pattern (the gray solid line) in the focal plane was obtained when the incident beam was located in the center of the objective lens. Two pairs of particles marked with white dashed circles at both the ends of the optical line trap moved automatically towards each other, and stopped when they reached the middle marked with a blue dot. The corresponding time sequences are highlighted in the left of the images. It can be deduced that these particles were driven to move automatically by the phase gradient force of the beam, and the fashion of the movement is in good agreement with the phase gradient distribution in the simulation.

We further demonstrated the beam patterns in the focal plane, which are corresponding to the cases of the input beam incident to the upper or lower parts of the objective lens, respectively. As shown in Figs. 5(e) and 5(f), particles moved unidirectionally from the right to the left and vice versa, which revealed that the focused beam possessed the unidirectional phase gradients. Based on Fig. 5, we quantified the velocities of particles along the phase gradients. Through the left to right movements in the experiments, we calculated out that the velocities of the particles were about 0.95 μm/s and 1.77 μm/s, respectively, which proved that different phase gradient distributions correspond to different velocities. By comparing the velocities, we found that the particles were almost two times faster when the phase gradient was nearly two times greater. It is worth mentioning that the moving speed of particles depends on not only the power of the laser, but also the factors such as the reconstructed beam quality, viscosity of the fluid, refractive indices of the particles, and the profile of the gradient phase distribution. Furthermore, the alignment between the orientations of the linear polarization and the line pattern also affects the coupling efficiency of the linear polarization and the gradient phase. From the experimental results we can find that the trajectories of the particles are consistent with the phase gradient distributions of the tightly focused linearly polarized line-shaped beam in the simulation. Both the simulation and experimental results confirm that the coupling between linear polarization and gradient phase can occur in a tight focusing process. Moreover, we deduce that the coupling between elliptical polarization and helical phase may also exist as a more general case, which needs to be investigated further.

IV. CONCLUSIONS

In summary, we have found the phenomenon that linearly polarized beam could be converted into gradient phase in a tightly focused process, which was verified by numerical simulations and experiments. The coupling further reveals the relationship of polarization and phase, and indicates that both the circular polarization-to-vortex phase conversion and the linear polarization-to-phase gradient conversion are special cases of the polarization-phase coupling.

ACKNOWLEDGMENTS

This research was financially supported by the National Natural Science Foundation of China (NSFC) (Grant No. 11674401) and the Natural Science Foundation of Hunan Province, China (Grant No. 2019JJ40358).

[1] A. T. O'Neil, I. MacVicar, L. Allen, and M. J. Padgett, Phys. Rev. Lett. **88**, 053601 (2002).
[2] H. He, M. E. J. Friese, N. R. Heckenberg, and H. Rubinsztein-Dunlop, Phys. Rev. Lett. **75**, 826 (1995).
[3] V. Garces-Chavez, D. McGloin, M. J. Padgett, W. Dultz, H. Schmitzer, and K. Dholakia, Phys. Rev. Lett. **91**, 093602 (2003).
[4] S. Tao, X. Yuan, J. Lin, X. Peng, and H. Niu, Opt. Express **13**, 7726 (2005).
[5] L. Marrucci, C. Manzo, and D. Paparo, Phys. Rev. Lett. **96**, 163905 (2006).
[6] B. Roy, N. Ghosh, S. DuttaGupta, P. K. Panigrahi, S. Roy, and A. Banerjee, Phys. Rev. A **87**, 043823 (2013).
[7] K. Y. Bliokh, F. J. Rodriguez-Fortuno, F. Nori, and A. V. Zayats, Nat. Photonics **9**, 796 (2015).
[8] Y. Fang, M. Han, P. Ge, Z. Guo, X. Yu, Y. Deng, C. Wu, Q. Gong, and Y. Liu, Nat. Photonics **15**, 115 (2021).

[9] Z. Zhang, C. Min, Y. Fu, Y. Zhang, W. Liu, and X. Yuan, Opt. Express **29**, 6282 (2021).
[10] Y. Liu, Y. Hwang, G. Si, Q. Wang, and D. Wang, Appl. Phys. Lett. **118**, 161106 (2021).
[11] E. Karimi, S. A. Schulz, I. D. Leon, H. Qassim, J. Upham, and R. W. Boyd, Light Sci. Appl. **3**, e167 (2014).
[12] R. C. Devlin, A. Ambrosio, D. Wintz, S. L. Oscurato, A. Y. Zhu, M. Khorasaninejad, J. Oh, P. Maddalena, and F. Capasso, Opt. Express **25**, 377 (2017).
[13] D. L. P. Vitullo, C. C. Leary, P. Gregg, R. A. Smith, D. V. Reddy, S. Ramachandran, and M. G. Raymer, Phys. Rev. Lett. **118**, 083601 (2017).
[14] Y. Zhao, J. S. Edgar, G. D. M. Jeffries, D. McGloin, and D. T. Chiu, Phys. Rev. Lett. **99**, 073901 (2007).
[15] D. Pal, S. D. Gupta, N. Ghosh, and A. Banerjee, APL Photonics **5**, 086106 (2020).
[16] Y. Qin, L. Zhou, L. Huang, Y. Jin, H. Shi, S. Shi, H. Guo, L. Xiao, Y. Yang, C. Qiu, and Y. Jiang, Nat. Commun. **12**, 3722 (2021).
[17] B. Chen and J. Pu, Appl. Opt. **48**, 1288 (2009).
[18] L. Fang, H. Wang, Y. Liang, H. Cao, and J. Wang, Phys. Rev. Lett. **127**, 233901 (2021).
[19] Y. Roichman, B. Sun, Y. Roichman, J. Amato-Grill, and D. G. Grier, Phys. Rev. Lett. **100**, 013602 (2008).
[20] Z. Yuan and S. Tao, J. Opt. **16**, 105701 (2014).
[21] S. Tao and W. Yu, Opt. Express **23**, 1052 (2015).
[22] L. Wu, S. Cheng, and S. Tao, J. Opt. **17**, 125603 (2015).
[23] S. Cheng, T. Xia, M. Liu, S. Xu, S. Gao, G. Zhang, and S. Tao, Opt. Laser. Technol. **113**, 266 (2019).
[24] K. Niu, D. Bao, and S. Tao, Opt. Commun. **458**, 124842 (2020).
[25] M. E. Friese, T. A. Nieminen, N. R. Heckenberg, and H. Rubinsztein-Dunlop, Nature (London) **394**, 348 (1998).
[26] Z. Cheng, P. M. Chaikin, and T. G. Mason, Phys. Rev. Lett. **89**, 108303 (2002).
[27] T. Wohland, A. Rosin, and E. H. K. Stelzer, Optik **102**, 181 (1996).
[28] K. D. Bonin, B. Kourmanov, and T. G. Walker, Opt. Express **10**, 984 (2002).
[29] P. Galajda and P. Ormos, Opt. Express **11**, 446 (2003).
[30] F. Nan and Z. Yan, Nano Lett. **20**, 2778 (2020).
[31] M. Gu, *Advanced Optical Imaging Theory* (Springer, Berlin, 2000), Vol. 75.
[32] E. Wolf, Proc. R. Soc. London Ser. A **253**, 349 (1959).
[33] A. Boivin and E. Wolf, Phys. Rev. **138**, B1561 (1965).
[34] K. Jahn and N. Bokor, Opt. Commun. **283**, 4859 (2010).
[35] K. Niu, S. Zhao, S. Tao, and F. Wang, Sens. Actuator A Phys. **333**, 113223 (2022).
[36] See Supplemental Material at http://link.aps.org/supplemental/10.1103/PhysRevA.106.043506 for the experimental videos.